Synthesis and structural and optical characterization of $APbX_3$ (A = MA, DMA, and TMA; X = I, Br) systems

Alessandro Mancini,[a] Paolo Quadrelli[a], Giuseppe Amoroso,[a] Chiara Milanese[a], Massimo Boiocchi[b],

Angelo Sironi[c], Maddalena Patrini[d], Giorgio Guizzetti[d] and Lorenzo Malavasi[a,*]

[a]*Department of Chemistry and INSTM, University of Pavia, Pavia 27100, IT*
[b]*University of Pavia, Centro Grandi Strumenti, 27100 Pavia, Italy*
[c]*University of Milano and INSTM, Via Golgi 19, 20133 Milano, Italy*
[d]*University of Pavia and CNISM, Via Bassi 6, 27100 Pavia, Italy.*

ABSTRACT

In this paper we report the synthesis, the crystal structure and the optical response of $APbX_3$ (A = MA, DMA, and TMA; X = I, Br) hybrid organic-inorganic perovskites including some new phases. We observe that as the cation group increases in size, the optical absorption edge shifts to higher energies with energy steps which are systematic and independent on the anion. A linear correlation between the optical bad gap and the tolerance factor has been shown for the series of samples investigated.

Corresponding Author: Prof. Lorenzo Malavasi; email: lorenzo.malavasi@unipv.it; tel.: +39-382 987921; fax; + 39 382 987575.

INTRODUCTION

Hybrid organic-inorganic perovskites of general formula ABX_3, where A is a protonated amine, B is a divalent metal (usually Ge^{2+}, Sn^{2+}, Pb^{2+}) and X is a halide, are known since long time in the field of solid state chemistry.[1] Such hybrid structures open important possibility of combining useful properties coming from the two different chemical entities. In addition, the extension of the well-established tuning strategies of inorganic perovskites to the hybrid systems, may pave the way to fascinating and intriguing structure-properties modulations in organic-inorganic perovskites. As a matter of fact, recently, Cheetam and co-workers, have suggested the use of Goldschmidt's concept of ionic Tolerance Factor in the field of hybrid perovskites.[2,3]

After the first report of the use of methylammonium lead iodide ($MAPbI_3$) perovskite in a solar cell[4], with an efficiency around 4%, the solar energy conversion efficiency for a device based on this material has reached 20% in November 2014.[5]

Most of the actual research on hybrid organic-inorganic perovskites focuses on the $MAPbI_3$ due to its excellent performance in devices. However, there is a significant interest in studying new materials both for practical applications (for example, to overcome the stability problems of $MAPbI_3$, tune the physical properties for tandem solar cells applications, etc) and fundamental science (*e.g.*, define the role of cation and/or anion substitutions on the physical properties).[6]

In the present paper we explored the role of protonated amine cation A on the $APbX_3$ system (X = I, Br, and Cl). In particular, we investigated the effect on the structural and optical properties of increasing the number of methyl groups linked to the aminic nitrogen of cation A, *i.e.* by considering methylammonium (MA), dimethylammonium (DMA) and trimethylammonium (TMA) cations.

2

EXPERIMENTAL

Samples of formula $APbX_3$ (A = MA, DMA, and TMA; X = I, Br, and Cl) have been synthesised according to a general procedure we developed, different with respect to the usual synthetic procedures used for hybrid organic-inorganic perovskites. In a typical synthesis, a proper amount of Pb acetate is dissolved in an excess of the desired HX acid under nitrogen atmosphere and stirring. The solution is heated to 100°C and the corresponding amine solution (25-40% in water) is added in equimolar amount. Usually, a precipitate is formed immediately after the amine addition. The solution is then cooled down to 46°C at 1°C/min, and the precipitate is immediately filtered and dried under vacuum overnight. The samples have been then characterized for their structural and optical properties. For the chlorinated $APbX_3$ samples, only with MA cation it was possible to obtain a single phase material. Most probably, the too big lattice mismatch between Cl^- and DMA and TMA cations is the main reason for this result.

Crystal structure analysis. Diffraction data for pale yellow single crystal of $DMAPbI_3$ were collected at room temperature with $Mo_{K\alpha}$ X-radiation (λ = 0.71073 Å) on a conventional Enraf-Nonius CAD4 diffractometer. Crystal data for $DMAPbI_3$: $C_2H_8I_3NPb$, M_r = 633.98, T = 293 K, dimensions 0.36 x 0.14 x 0.12 mm^3, hexagonal, $P6_3/mmc$ (No. 194), a = 8.7693(15) Å, c = 8.1886(18) Å, V = 545.3(3) $Å^3$, Z = 2, ρ_{calcd} = 3.861 g cm^{-3}, $F(000)$ = 536, μ $Mo_{K\alpha}$= 23.891 mm^{-1}, θ_{max} = 30°, 0.076/0.162 min/max transmission factors, 4137 measured reflections, 338 independent reflections (R_{int} = 0.041), 286 strong reflections [$I_O > 2\sigma(I_O)$], 13 refined parameters, R_1 = 0.0326 (strong data) and 0.0406 (all data), wR_2 = 0.0707 (strong data) and 0.0760 (all data), GOF = 1.177, 0.78 and -1.39 max. and min. electron density residuals.

Data reduction was performed with the WinGX package[23]. Intensities were corrected for Lorentz and polarization effects; absorption effects were evaluated with the ψ-scan method[24] and absorption correction was applied to the data. Crystal structure was solved by direct methods (SIR 97)[25] and refined by full-matrix least-squares procedures on F^2 using all reflections (SHELXL-2014).[26] Anisotropic displacement parameters were used for Pb, I and fully populated C atom sites, whereas the partly populated C and N atom sites were refined isotropically. Hydrogens were placed at calculated positions and their positions refined accordingly to a riding model.

The N atom of the DMA moiety in the DMAPbI₃ crystal is placed in a special position a third populated. This arrangement defines three different orientations of the DMA moieties, mutually exclusive and statistically distributed.

X-Ray Powder Diffraction

Gently ground powders of TMAPbX₃ (X = Br, I) compounds were deposited in the, 2 mm deep, hollow of a zero background plate (a properly misoriented quartz monocrystal). Diffraction experiments were performed using Cu-Kα radiation (λ = 1.5418 Å) on a vertical-scan Bruker AXS D8 Advance diffractometer in θ:θ mode, equipped with a Goebel Mirror and a linear Position Sensitive Detector (PSD), with the following optics: primary and secondary Soller slits, 2.3 and 2.5°, respectively; divergence slit, 0.1°; receiving slit, 2.82°. Generator setting: 40 kV, 40 mA. The nominal resolution for the present set-up is 0.08° 2θ (FWHM of the α₁ component) for the LaB6 peak at about 21.3° (2θ).

The accurate diffraction patterns at RT of TMAPbX₃ (X = Br, I) compound were acquired in the 5-90° 2θ range, with Δ2θ = 0.02° and exposure time 4 s/step.

TMAPbI₃: indexing of the predominant peaks (all but a bunch of very small ones accounting for much less than 1% of the diffracted intensity, see Figure **S2**) was performed with the aid of the

single value decomposition approach,[27] as implemented in the TOPAS-R suite of programs,[28] leading to a trigonal/hexagonal cell of approximate dimensions: a = b = 9.268 Å and c = 8.041 Å resembling that of the DMAPbI$_3$ derivative. Accordingly, we assumed the very same $P6_3/mmc$ (No. 194) space group. A Le Bail refinement led to an Rwp of 14.0 (see Figure **S2**) while assuming also the related structural model (Pb and I atoms only) we obtained a reasonable fit of the intensities with R_p, R_{wp}, R_{Bragg} equal to 16.2, 23.5 and 11.7, respectively (see Figure **S3**). A better fit, with R_p, R_{wp}, R_{Bragg} equal to 13.3, 20.1 and 7.7, respectively, (see Figure **S4**) is obtained by disordering the Iodine atoms into *j* Wickoff positions (in the DMAPbI$_3$ ordered model the Iodine atoms sit on *h* Wickoff positions). A last, considering also the presence of disordered TMA cations about *c* Wickoff positions, we obtain a quite reasonable final fit with R_p, R_{wp}, R_{Bragg} equal to 9.5, 14.7 and 3.8, respectively (see Figure **3**).

TMAPbBr$_3$: the same procedure followed for TMAPbI$_3$ led to a hexagonal cell of approximate dimensions: a = b = 8.873 Å and c = 7.706 Å. The Le Bail refinement, in $P6_3/mmc$, failing to describe only a few very small peaks accounting for less than 1% of the diffracted intensity (see Figure **S6**), afforded an R_{wp} of 13.0. The refinements of the ordered and disordered structural models showed a similar behaviour as those for TMAPbI$_3$. Eventually, the final Rietveld refinement of the structure consisting of disordered chains and disordered cations led to R_p, R_{wp}, R_{Bragg} equal to 9.3, 13.6 and 3.3, respectively (see Figure **S7**).

Peak shapes were described by the fundamental parameters approach.[29] The experimental background was fit by a polynomial description. Systematic errors were modelled with sample-displacement angular shifts corrections. A common, refinable, isotropic displacement parameter was assigned to all atoms. Scattering factors, corrected for real and imaginary anomalous dispersion terms, were taken from the internal library of TOPAS. **Crystal data for TMAPbI$_3$ compound:** C$_3$H$_{10}$I$_3$NPb, fw = 647.6 g mol^{-1}, hexagonal $P6_3/mmc$ (No. 194), a = b = 9.2579(3) and c = 8.0333(4) Å, V = 596.28(5) Å^3, Z = 2, ρ_{calc} = 3.55 g cm^{-3}, μ(Cu-Kα) = 875.73 cm^{-1}. R_p and R_{wp} = 9.5 and 14.7, respectively, for 4251 data collected in the 5-90° 2θ range. R_{Bragg} = 3.8.

Crystal data for TMAPbBr₃ compound: $C_3H_{10}Br_3NPb$, fw = 506.6 g mol⁻¹, hexagonal *P6₃/mmc*

(No. 194), a = b = 8.8732(2) and c = 7.7067(3) Å, V = 525.49(3) Å³, Z = 2, ρ_{calc} = 3.14 g cm⁻³, μ(Cu-

Kα) = 433.35 cm⁻¹. R_p and R_{wp} = 9.3 and 13.6, respectively, for 4251 data collected in the 5-90° 2θ

range. R_{Bragg} = 3.3.

CCDC 1408123, 1408124 and 1408124 contain the supplementary crystallographic data for

this paper.

Diffuse Reflectance Spectra

The optical diffuse reflectance spectra of the different perovskites were measured from 0.8 to

4.5 eV (250-1500 nm, with steps of 1 nm) by a Varian Cary 6000i equipped with an integrating

sphere. For this kind of measurements polycrystalline powders were compacted into pellets

of about 20 mm in diameter and reflectance spectra were calibrated using a standard reference

disk.

RESULTS

In the following sections are presented the results of the investigation carried out on the CuO

thin films deposited under different experimental conditions. For sake of clarity, the results will be

organized as a function of the deposition parameter varied during the growth of the CuO films.

Substrate Temperature Effect on Structure and Morphology

A first series of copper oxide thin films was grown by changing the substrate temperature from no-heating (indicated as RT) to 700°C (100, 200, 300, 400, 500, 600 and 700°C). As can be seen from Table 1, the other sputtering parameters were kept fixed (*i.e.*, total pressure = 4.3 · 10^{-5} bar, Ar flux = 20 sccm, O$_2$ flux = 5 sccm, RF-power = 200 W). Deposition time was 15 minutes for all the films.

Figure 1 reports the x-ray diffraction (XRD) patterns for the series of thin films deposited as a function of increasing substrate temperature. Vertical red bars refer to the reference pattern for the monoclinic tenorite CuO phase.
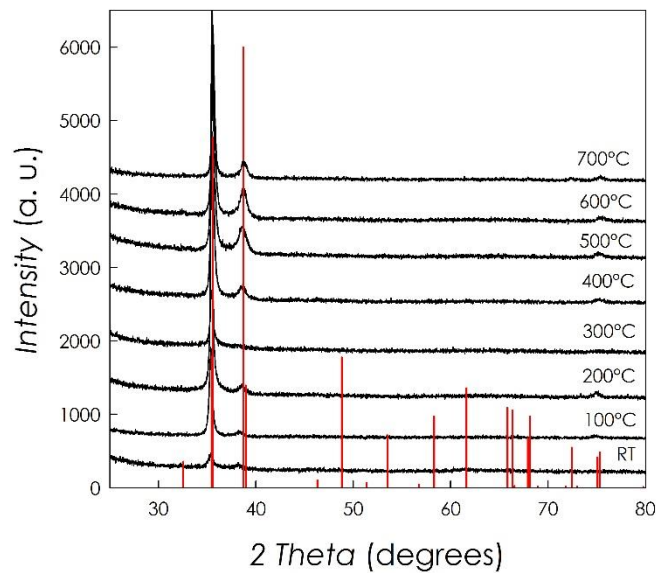

Fig. 1 – XRD patterns for the CuO thin films grown at different substrate temperatures. Vertical red bars refer to the reference pattern for the tenorite CuO.

From Figure 1 it is possible to observe that the CuO thin films are single-phase and their XRD patterns are consistent with the expected tenorite crystal structure. In addition, a significant orientation of the films is as well evident from the reported patterns where the strongest reflection around 35° corresponds to the (-111) Bragg peak. A second less intense peak (~38.5°) pertains to the (111) reflection which, however, should be the most intense reflection based on the calculated pattern

(see vertical red bars). There is not a clear and simple dependence of the relative intensities of the two diffraction peaks observed as a function of the deposition temperature but it can be concluded that the deposited thin films are strongly oriented along the (-111) direction with a complete iso-orientation for the film deposited at 300°C. This peculiar growth direction has been also observed in previous reports [48, 49] on the RF-sputtering deposition of CuO thin films. However, Gosh et al. [48] could observe the formation of pure CuO only above 300°C (while at lower temperatures Cu_2O was the main phase) and Lim et al. found Cu-impurities in most of the deposited thin films, for similar deposition conditions [49].

In Figure 2 is reported the position of the peak around 35°, *i.e.*, the (-111) reflection, as a function of the substrate temperature during the CuO film deposition. Horizontal red line corresponds to the position of the (-111) reflection in bulk CuO.
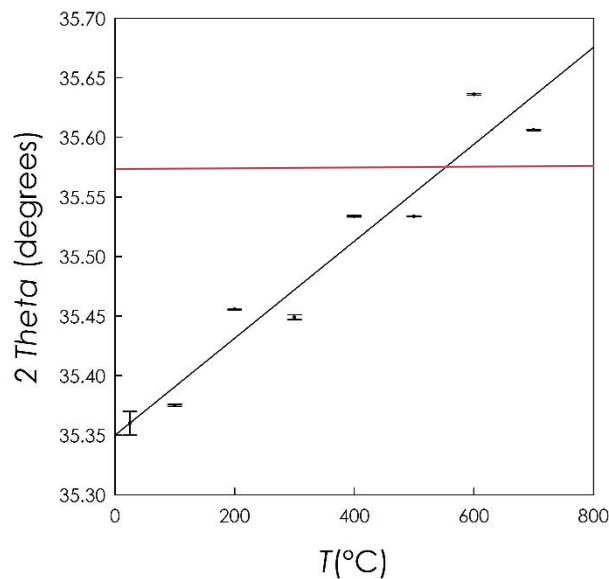

Fig. 2 – Position of the most intense peak in the patterns as a function of substrate temperature. Red line represents the CuO bulk value of the (-111) reflection.

From Figure 2 it is possible to observe a general progressive shift of the diffraction peak towards higher angles by increasing the substrate temperature; this in turn implies a progressive contraction

of the unit cell by increasing *T*. This behavior could be correlated to both a partial change of Cu oxidation state (due, for example, to oxygen non-stoichiometry) and/or to microstructural effects such as lattice strain.

To probe the Cu oxidation state in the deposited CuO films, XPS measurements have been performed on the two samples deposited at the lowest (RT) and highest (700°C) substrate temperature. Figure 3 reports the Cu-2*p* and O-1*s* spectra for the above mentioned films.
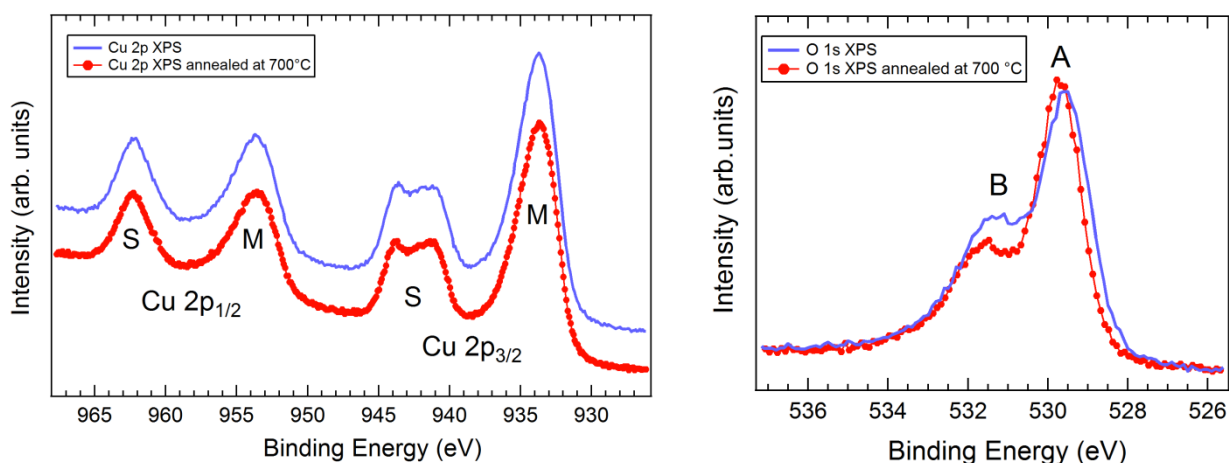

Fig. 3 – Cu-2p and O-1s spectra for the CuO thin films deposited with the substrate kept at RT and 700°C.

Peaks shape and position for the two films, which represent the lower and higher limit of the substrate temperature series, are very close each other, and the Cu-2*p* XPS spectra confirm that Cu is present in the +2 oxidation state. Indeed, the Cu 2p core lines show the spin-orbit split peaks in the 930-947 eV binding energy (BE) range for the Cu $2p_{3/2}$ component and in the 947-967 eV BE range for the Cu $2p_{1/2}$ component. Each spin orbit split contribution shows a main line (M) at lower BE and a satellite (S) at higher BE. These spectra are characteristic of the Cu^{2+} emission, being the main line mainly related to the charge-transfer screened $\underline{2p}3d^{10}\underline{L}$ final state of the Cu^{2+} cation and the satellite to the atomic-like $\underline{2p}3d^9$ unscreened final state, where $\underline{2p}$ indicates the 2p core-hole in the final state, and $\underline{L}$ the O 2p hole related to the O 2p → Cu 3d charge transfer effect [53]. Slight changes upon annealing seem to involve the O 1s emission only. The main line (A) at BE=529.5 eV width reduces

9

upon annealing, and a reduction of the high BE shoulder (B) is observed after annealing. As this peak can be ascribed to the contribution of OH and O adsorbed [54] on the surface, we can conclude that annealing has partially contributed to reduce the species adsorbed on the surface.

As the electronic properties of Cu cations appear to be nearly identical from the surface sensitive XPS probe, if a change of oxidation state occurs as a function of the substrate temperature during deposition, this would be related to the bulk of the sample and not to the surface. However, this result also suggests that the significant peak shift observed in the diffraction pattern could be to microstructural/relaxation effects.

All the thin films deposited as a function of substrate temperature underwent AFM investigation in order to define their surface morphology. The results for the 5 µm × 5 µm scans are reported in Figure 4.
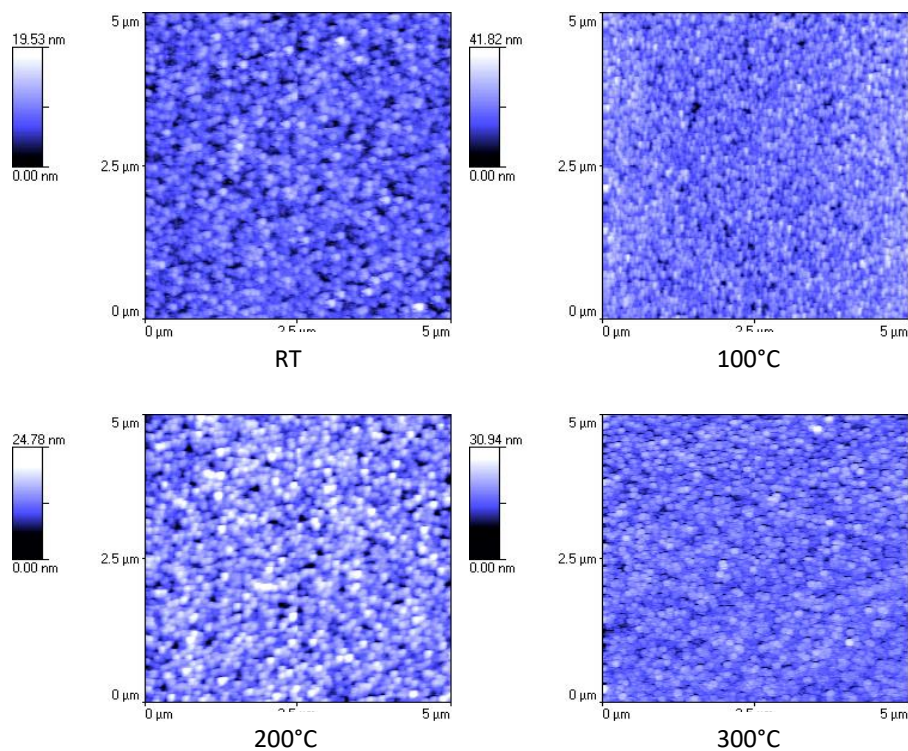
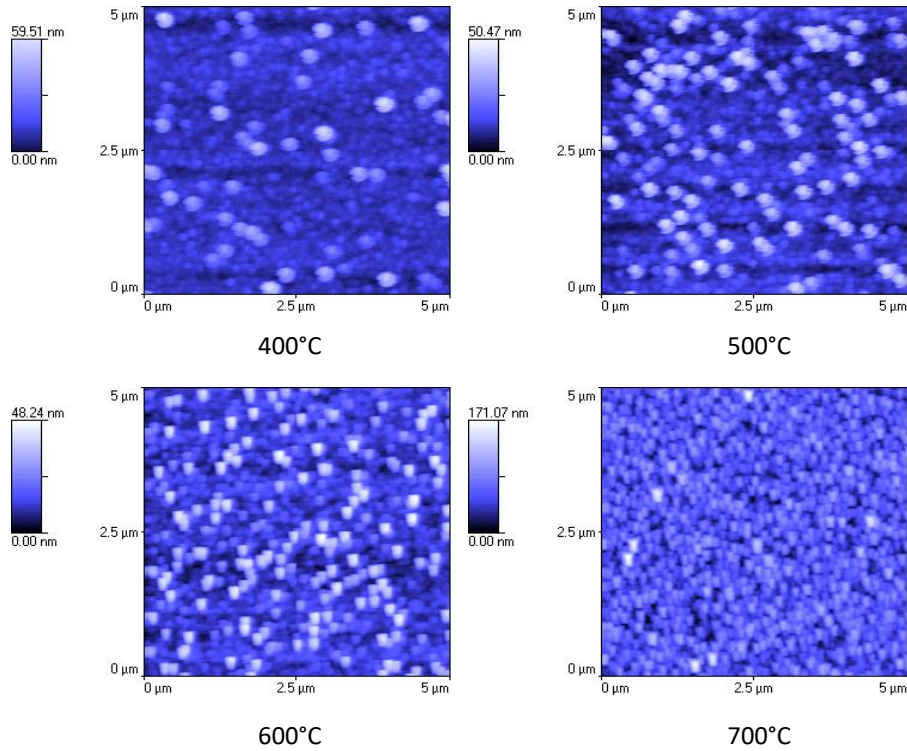*Fig. 4 – 5 μm × 5 μm AFM scans for the CuO thin films deposited at different substrate temperatures.*

Overall, the AFM scans reveal the presence of nanosized grains with a nearly spherical shape for all the substrate temperatures. The average grain size (*e.s.d.* ±10 nm) and surface roughness (R_{rms}) calculated from the AFM scans are reported in Table 2.

Table 2 – Average grain size and surface roughness determined from the AFM scans for the CuO thin films deposited at different substrate temperatures.

Substrate Temperature (°C)	Average Grain Size (nm)	R_{rms} (nm)
RT	150	2.5(2)
100	160	4.1(1)
200	150	3.2(3)
300	110	3.1(6)
400	115	8.5(5)
500	220	8.6(2)
600	218	8.2(1)
700	220	20.7(5)

Root mean square surface roughness indicate very smooth films with a tendency of R_{rms} to increase with the substrate temperature. In general the roughness is below 10 nm for all the substrate

temperatures except for the film deposited at 700°C where it reaches a value around 20 nm. Such R_{rms} values are in agreement with previous literature reporting AFM investigation for a limited set of substrate temperatures [46, 47]. The presence of a sharp roughening transition in the range 600°-700°C is compatible with a columnar growth mechanism, which is expected to hold for $T/T_m<0.5$ (where T is the substrate temperature and T_m is the melting temperature of the bulk material) [55-57].

In order to get some information on the films density and the growth mechanism, on some selected samples a SEM investigation has been performed. Figure 5 reports the SEM images (lateral section) for the CuO thin films grown with a substrate temperature of 300 and 600°C, as selected examples.
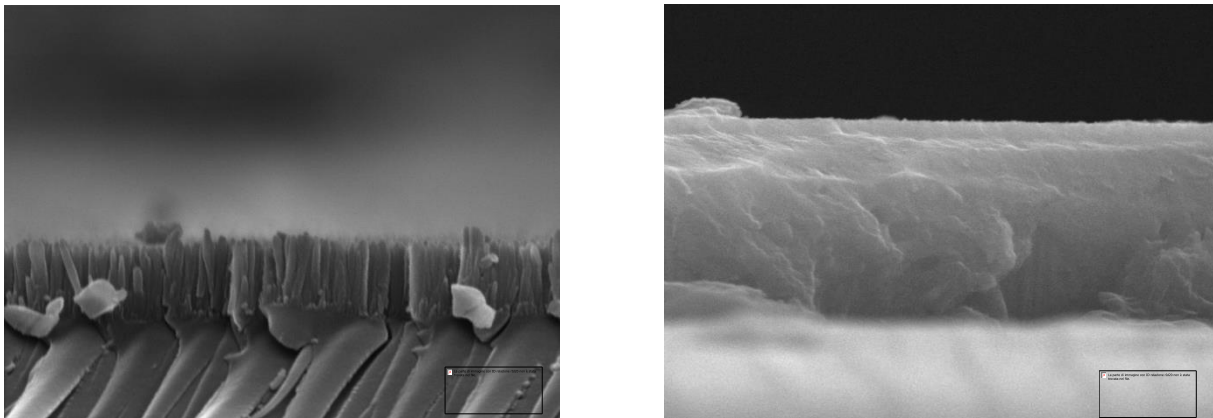

Fig. 5 – SEM images for the CuO thin films deposited at 300°C (left) and 600°C (right).

The SEM images suggest a columnar growth characterized by the presence of vertical well-aligned nanorods, which is more evident and clear for the CuO film deposited at 300°C while for the film deposited at 600°C clear nanorods are only seen in some parts of the sample. Also, the structure looks denser by increasing the substrate temperature as a consequence of the higher mobility of the adatoms on the film surface.

RF Power Effect on Structure and Morphology

A second series of copper oxide thin films was grown by changing the RF power from 100 W to 300 W (100, 200 and 300 W) while keeping fixed the following sputtering parameters: substrate temperature = 300°C, total pressure = $4.3 \cdot 10^{-5}$ bar, Ar flux = 20 sccm, O_2 flux = 5 sccm). Deposition time was 15 minutes for all the films.

Figure 6 reports the XRD patterns collected on the three films deposited at the three different RF power values.
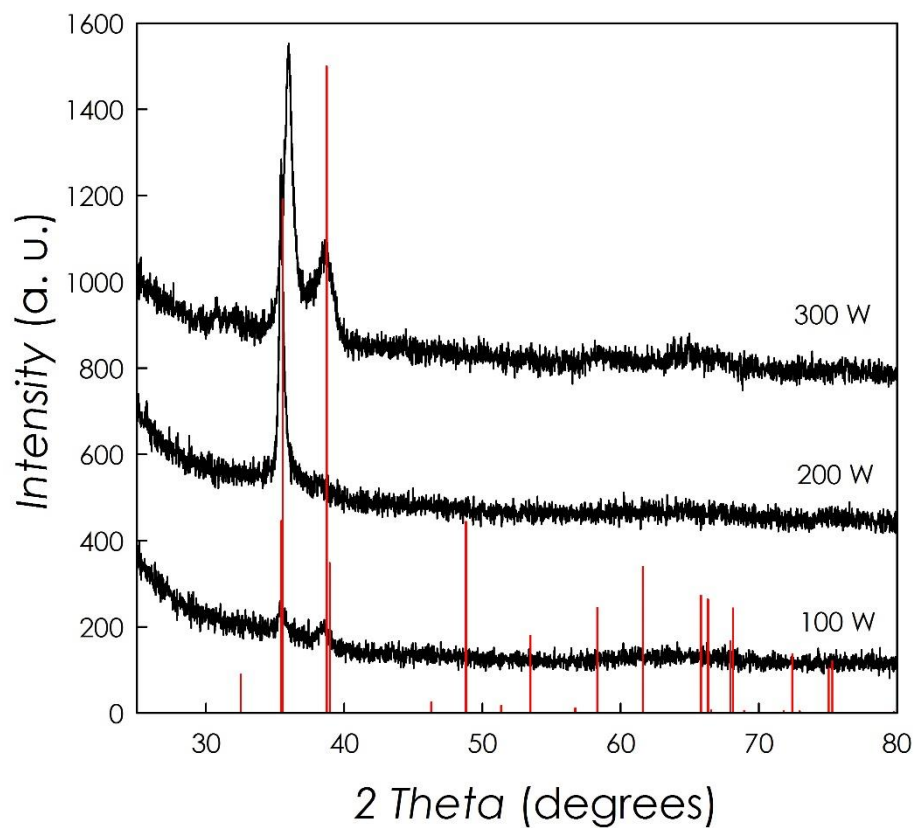

Fig. 6 – XRD patterns for the CuO thin films grown at different RF power values. Vertical red bars refer to the reference pattern for the tenorite CuO.

These results confirm that the thin films have been grown as single-phase materials at each RF power value and with the monoclinic tenorite crystal structure. As for the case of the thin films series grown at different substrate temperatures, a significant orientation of the films is as well evident from the reported patterns. From the diffraction data it was possible to observe a significant shift at

higher angle of the main diffraction peak (the one located around 35°) passing from the films deposited at 100 and 200 W (ca. 35.45°) to the film deposited at 300 W (35.96°), thus suggesting a cell contraction. Lim et al. [45] reported the deposition of copper oxides thin films by means of RF sputtering employing analogous deposition conditions and by changing the RF power. With respect to their results, where multi-phase films composed of CuO and Cu_2O were obtained, we could successfully grow single-phase CuO films.

AFM investigation of the deposited thin films is reported in Figure 7 showing a spherical-like shape for all the samples with a progressive increase of both grain size and roughness by increasing the RF power employed during the film deposition.
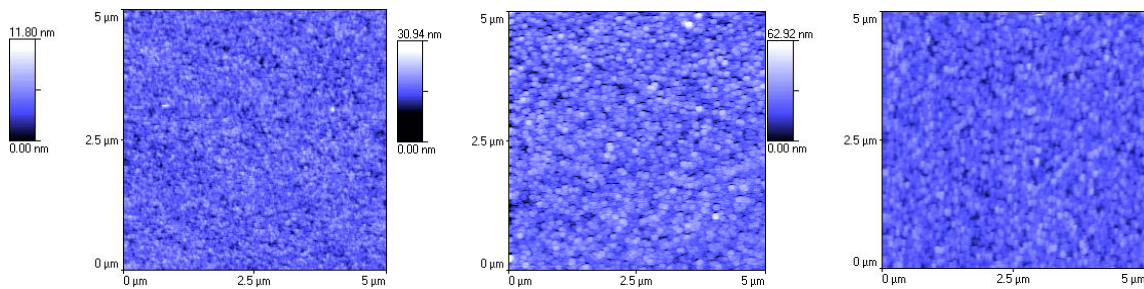

Fig. 7 – 5 µm × 5 µm AFM scans for the CuO thin films deposited at different RF power values.

14

The grain size and average surface roughness for the three thin films are shown in Figure 8.
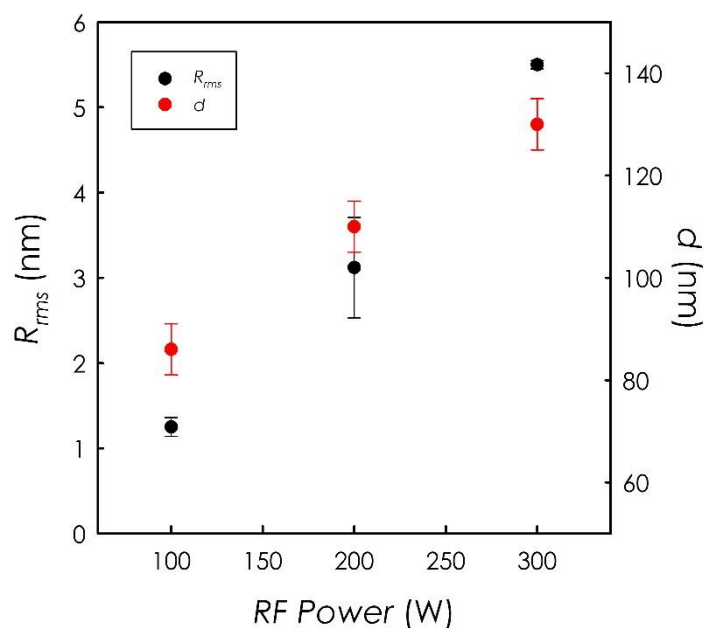

Fig. 8 – Trend of surface roughness and grain size for the CuO thin films deposited at different RF power values.

A clear trend is seen from Figure 8 with the average grain size and roughness increasing by increasing the RF power during thin films deposition. This is due to the fact that an increase in the RF power causes an increase in the energy of the Ar^+ ions when they collided with the target resulting in an increase in the surface mobility of the sputtered particles. The SEM investigation (not shown) reveals a clear columnar growth for the CuO films grown at lower RF power values while a denser and more compact lateral structure for the film deposited at 300 W.

Oxygen Content Effect on Structure and Morphology

The last series of CuO thin films was deposited by changing the oxygen content in the sputtering gas while keeping all the other parameters fixed (*i.e.*, substrate temperature = 300°C, total pressure = $4.3 \cdot 10^{-5}$ bar, RF power = 200 W). The list of the samples prepared is presented in Table

1. The amount of oxygen was changed from 15 to 70% relative to the total amount of O$_2$+Ar sputtering gas.

The effect of oxygen content variation on the thin films composition is shown in Figure 9 reporting the XRD patterns as a function of the O$_2$ percentage.
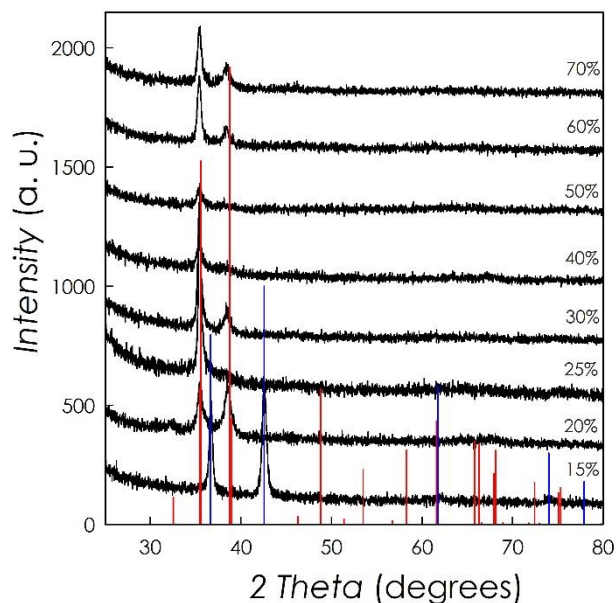

Fig. 9 – XRD patterns for the copper oxides thin films grown at different oxygen contents. Vertical red bars refer to the reference pattern for the tenorite CuO while vertical blue bars refer to the Cu$_2$O Bragg peaks.

From the inspection of the XRD patterns reported in Figure 9 it can be seen that when the oxygen amount is 15% in the sputtering gas mixture (O$_2$+Ar) the stable phase is Cu$_2$O, while for all the other oxygen contents single-phase tenorite CuO thin films are obtained. It is interesting to note that passing from 15% to 20% of O$_2$ amount we could selectively grow single phase Cu$_2$O and CuO, respectively, thus avoiding the formation of multi-phase thin films, as reported in literature [46]. An analysis of the position of the main peak of the CuO thin films (at about 35°) revealed a modest variation of the position along with the oxygen content, with all the peaks falling within 35.43±0.03. These are very small variations with respect to those observed by varying the substrate temperature or the RF power thus suggesting that the oxidation state of the copper ions in the CuO thin films is

+2 already at the lowest oxygen content stabilizing the CuO phase. This is also in agreement with the XPS data reported in the previous section.

Some selected AFM images of the deposited thin films are shown in the following Figure.
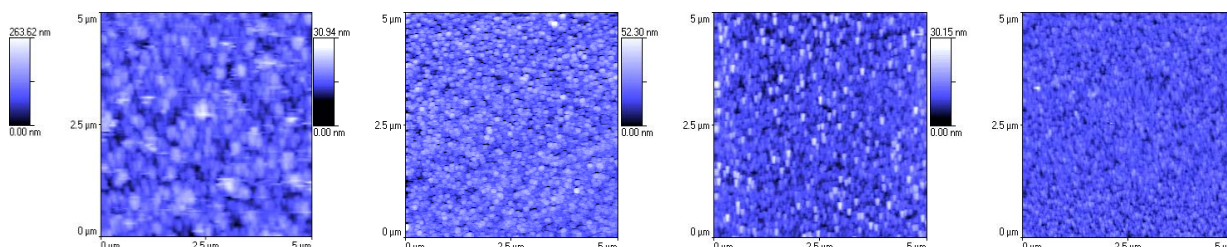

Fig. 10 – 5 μm × 5 μm AFM scans for the copper oxides thin films deposited at different oxygen contents. From left to right: 15, 25, 40 and 50%.
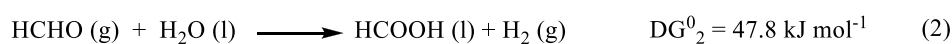
Average roughness of the CuO thin films are in the range of 3-6 nm while the Cu_2O (first image in Figure 10) has a significant higher R_{rms} of the order of 36.1(6) nm. In addition, while the average grain size of the three CuO thin films is within 100-150 nm (in agreement with the data shown previously), the grains of the Cu_2O are significantly larger, falling between 250 and 300 nm. SEM inspection (not shown) revealed a clear columnar growth up to 40% of oxygen content, while at higher concentrations the films look less well-defined in their lateral section and with a higher density.

Photocatalytic Activity

After the extensive study of the correlation between the deposition conditions and the structural and morphological properties of the nanostructured thin films grown, an investigation on the photocatalytic activity has been carried out. This was performed on selected CuO thin films according to preliminary consideration relative to the morphology, density, grain size and crystal structure in order to shed light on the most important characteristics affecting the photocatalytic

properties. All the measurements have been performed as described in the Experimental section by using a 1:1 water:methanol solution under irradiation with a conventional medium pressure Hg lamp. Photoreforming reactions have been carried out for 20 h in order to verify the materials stability as well.

Recently, the production of hydrogen has been extended to the photodecomposition of methanol (CH_3OH), which has a lower splitting energy than water. Sakata et al. [58-61] have described that the reaction can proceed either stepwise, involving stable intermediates such aldehydes and acids (Eqs. (1) and (3)).
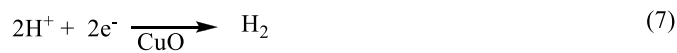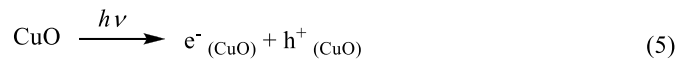
$$CH_3OH \text{ (l)} \longrightarrow HCHO \text{ (g)} + H_2 \text{ (g)} \qquad DG^0_1 = 64.1 \text{ kJ mol}^{-1} \qquad (1)$$

$$HCHO \text{ (g)} + H_2O \text{ (l)} \longrightarrow HCOOH \text{ (l)} + H_2 \text{ (g)} \qquad DG^0_2 = 47.8 \text{ kJ mol}^{-1} \qquad (2)$$

$$HCOOH \text{ (l)} \longrightarrow CO_2 \text{ (g)} + H_2 \text{ (g)} \qquad DG^0_3 = 95.8 \text{ kJ mol}^{-1} \qquad (3)$$

One step on the catalyst surface to give the overall reaction (Eq. (4)) has been reported by Chen et al. [62].

$$CH_3OH \text{ (l)} + H_2O \text{ (l)} \longrightarrow CO_2 \text{ (g)} + 3H_2 \text{ (g)} \qquad DG^0 = 16.1 \text{ kJ mol}^{-1} \qquad (4)$$
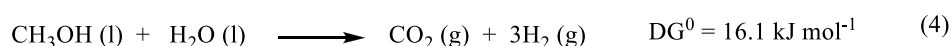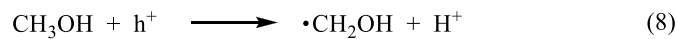
Hydrogen is produced in all of these steps. The water splitting reaction is endothermic and requires an input energy of 237 kJ/mol [63]. Methanol has a lower splitting energy relative to water. In Figure 11 a possible scheme of reactions, based on the literature [63, 64], is estimated in order to better understand the photocatalytic process of hydrogen formation from the aqueous methanol solution. The overall process can be divided into three steps. In the first step (Eqs. (5) and (7)), there exists a water-splitting process on the surface of CuO photocatalyst. The rate of water splitting is limited by accumulation of active photogenerated holes and, OH radicals. In second step (Eqs. (8) and (11)), the photogenerated holes attack methanol to form formaldehyde, which are further oxidized by both ,OH radicals and photogenerated holes to produce formic acid [65]. At third step (Eqs. (12)

and (14)), the formic acid is decarboxylated by the photo-Kolbe reaction to release CO_2 [66]. The H^+ deprotonated during whole process transfers to the loaded CuO particles and then reduce to hydrogen by the photogenerated electrons. However, actual mechanism must be more complicated, which relies on monitoring reactants, intermediates, products as well as radicals. Further investigations with the help of advanced instruments and in situ techniques are needed.

Step 1

$$CuO \xrightarrow{h\nu} e^-_{(CuO)} + h^+_{(CuO)} \qquad (5)$$

$$h^+ + H_2O \longrightarrow H^+ + \cdot OH \qquad (6)$$

$$2H^+ + 2e^- \xrightarrow{CuO} H_2 \qquad (7)$$

Step 2

$$CH_3OH + h^+ \longrightarrow \cdot CH_2OH + H^+ \qquad (8)$$

$$\cdot CH_2OH + h^+ \longrightarrow HCHO + H^+ \qquad (9)$$

$$2H^+ + 2e^- \xrightarrow{CuO} H_2 \qquad (10)$$

$$HCHO + \cdot OH + h^+ \longrightarrow H^+ + HCOOH \qquad (11)$$

Step 3

$$HCOOH \longrightarrow HCOO^- + H^+ \qquad (12)$$

$$HCOO^- + 2h^+ \longrightarrow H^+ + CO_2 \qquad (13)$$

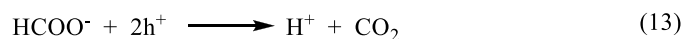$$2H^+ + 2e^- \xrightarrow{CuO} H_2 \qquad (14)$$

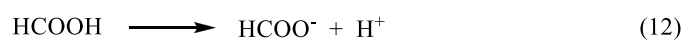Fig. 11– Photocatalytic reaction for hydrogen production from aqueous methanol solution in the proposed mechanism

The CuO nanostructured thin films, which underwent the photocatalytic test, are reported in the following table.

Table 3 – Deposition parameters for the *CuO* thin films which underwent photocatalytic activity study

Sample	T_{sub} (°C)	Rf power (W)	O_2 amount (%)

1	RT	200	25
2	300	200	25
3	600	200	25
4	300	200	40
5	300	200	60
6	RT	100	25

Such selection of deposition conditions allowed to test the dependence of one single parameter at time on the catalytic properties: substrate temperature (RT, 300 and 600°C); oxygen content in the sputtering gas (25, 40 and 60%) and RF power value (200 and 100 W).

In addition, a replica of sample 2 (indicated as sample 7) was prepared followed by a further deposition of Ag nanoparticles (performed at RT by means of RF-magnetron sputtering starting form an Ag target) in order to increase the absorption in the visible spectral range and to improve the photocatalytic properties, as discussed in the previous sections. The Ag nanoparticles were deposited in form of isolated "islands" of tens of nanometers after the growth of the CuO films.

Figure 12 reports the H_2 evolution for all the CuO thin films tested and listed in Table 3. The data are normalized to the geometrical surface area of the samples.
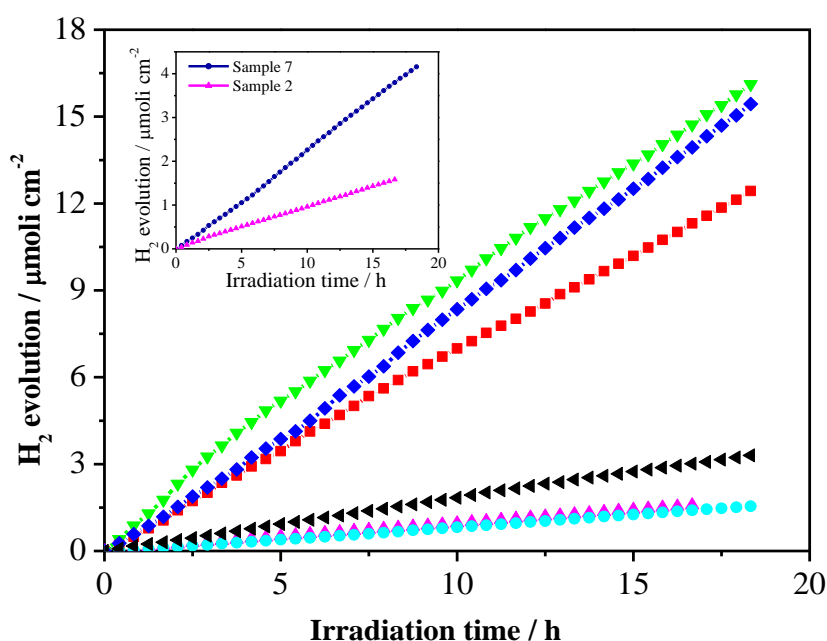
Fig. 12 – Hydrogen production as a function of time in photocatalytic experiments of methanol photo-dehydrogenation over CuO nanostructured thin film: Sample 1 (■)Sample 2 (▲) Sample 3 (●) Sample 4 (▼) Sample 5 (◆)Sample 6 (◄) In the inset the effect on photocatalytic activity of the functionalization with Ag-NPs Sample 7 (●).

.

The constant hydrogen production observed in Figure 12 suggests that all the CuO thin films tested are stable during the irradiation time (20 hrs). This is also confirmed by the visual inspection of the samples after the photocatalytic experiments showing no appreciable photocorrosion of the CuO layer, which is a potential problem for Cu based systems [67, 68]. Among the best performing samples, in terms of hydrogen evolution, it is possible to find sample 4 of Table 3, *i.e.* the one deposited at intermediate oxygen content among sample 2 (25%) and 5 (60%). With respect to these last two samples the H_2 evolution is significantly higher. As described in the pertinent section above, the grain size and nanostructure is very similar for the three thin films deposited at varying oxygen content. A more dense film is obtained at 60% of O_2 content with a less defined columnar growth which may explain the lover H_2 evolution for this sample. However, such difference is not found between the 25% and 40% films. The only significant difference between these two samples, that could account for the observed performances, is the higher level of iso-orientation, inferred from the XRD patterns of Figure 9, found for the CuO film grown at 40% of oxygen content. Such preferential growth may led to a greater activity related to the crystallographic plane exposed (-111).

Regarding the samples deposited at different substrate temperatures, that have been tested relative to the photocatalytic performance, the CuO film grown without substrate heating (n° 1) shows the best performance with respect to the samples grown at 300 and 600°C (samples n° 2 and 3, respectively). In this case, according to the investigation reported in the pertinent section, the low grain size, coupled to a better defined morphology of the nanostructure (characterized by aligned nanorods) and to a lower density results in a more efficient H_2 production. However, the nearly 10-fold improvement of the H_2 production for sample 1 with respect to sample 2 (grown in the same conditions but heating the substrate at 300°C), which have no drastic differences in terms of

morphology, may also be correlated to the structural properties reported in Figure 2. From the analysis of the XRD patterns we could observe an expansion of the lattice by reducing the substrate temperature during deposition, with the lowest position of the main peak (and thus bigger lattice) found for the CuO film grown at RT. Such expansion of the cell may be due to the presence of partially reduced Cu ions leading to an improvement of the catalytic activity.

The last CuO nanostructured thin film with an enhanced photocatalytic activity is a sample similar to the previous film (n° 1) but deposited at a lower RF power value of 100 W. This film shows a further enhanced H_2 production with respect to the film deposited at 200 W (and with the same remaining deposition parameters). As presented in Figure 8, by lowering the RF power the CuO film grows with a smaller grain size which is expected to improve the catalytic reaction with the sacrificial agent. Since the application of BET method is not trivial due to the impossibility to remove the cupper oxides films from the supporting substrate without altering their nature and due to the unavoidable and not negligible contribution of the substrate, an estimation of the surface area of the thin films has been done by means of AFM. Consistently with the morphology described in the previous section, relatively small values in the range 0.4-0.5 m^2/g where obtained, with no significant difference between the samples. This clearly indicates that surface area effects can be excluded. While the activity trend is scientifically interesting, the absolute Solar-to-Fuel efficiency are modest and varies from 0.02 to 0.07 % for the less to the most active sample. These compact supported CuO materials are less active with respect to more reactive branched nanowires CuO structures [69] where, under similar working conditions, an H_2 evolution of about 3 L h^{-1} m^{-2} where observed, which is nearly one order of magnitude higher than the 0.4 L_{H2} h^{-1} m^{-2} observed for the present best sample. This observation strongly highlights the importance of open nanostructure in driving both photo-activity and stability/resistance against mechanical stresses induced by the formation of hydrogen bubbles. However, it should be remarked that the photo-activity of the nanostructured thin films reported here,

prepared by means of sputtering, while not yet optimal, is a very appealing starting point within the framework of a cost-effective and scalable method.

Finally, an interesting comparison can be done for films n° 2 and 7 which have been grown under the same conditions but further functionalizing film n° 7 with Ag nanoparticles. As can be seen from Figure 12, the H_2 evolution has been improved of about 4 times in the film where Ag nanoparticles were present. Similar beneficial effects due to the presence of Ag were previously reported [70, 71].

CONCLUSIONS

In this paper we have carried out an extensive study relative to the deposition of CuO thin films by means of RF-magnetron sputtering starting from a Cu metal target and varying (once at time) three deposition parameters: i) substrate temperature; ii) RF-power, and iii) oxygen content in the sputtering gas. All the films deposited were single phase materials of tenorite CuO except for the lowest oxygen partial pressure used in the depositions which led to the growth of single phase Cu_2O.

The extensive structural, morphological, and photocatalytic activity characterization allowed to put in prominence the parameters that seems to mostly affect the catalytic properties of CuO films. In particular, even though all the deposited films show a nanostructure composed of nanorods of variable diameter between 80 and 200 nm, those conditions that lead to the growth of well aligned rods, *i.e.* relatively low substrate temperatures and from low to intermediate oxygen partial pressures, resulted in more efficient catalytic activities. It is also clear that a reduction in the diameter of the rod down to 100 nm improves the photocatalysis and this effect seems to be more relevant than the variation of the film roughness. Finally, our investigation suggests a relevant role of the crystallographic orientation of the CuO tenorite film on the catalytic activity, as demonstrated by the significant improvement in the H_2 evolution for highly oriented films. Within the framework of the

films and parameters investigated in this work, the relevance of the proper choice of the growth conditions is very significant, with photocatalytic activity improvements of more than 10 times for the best performing nanostructured films with respect to the less active samples. Finally, it should be stressed that the photo-activity results reported here are related to films grown with a cost-effective and scalable process which can open the way to real large-scale applications. Further work is planned in order to improve the photocatalytic activity of RF-sputtered CuO thin films.

Moreover, since the photocatalytic mechanism of most metal oxides used in the photoreforming reaction is similar, the guidelines unveiled in this work might be extended to other systems thus providing a guide to grow more efficient metal oxides nanostructured thin films.

ACKNOWLEDGEMENTS

REFERENCES

[1] S. Zinoviev, F. Muller-Langer, P. Das, N. Bertero, P. Fornasiero, M. Kaltschmitt, G. Centi, S. Miertus, *ChemSusChem*, 2010, **3**, 1106.

[2] M. G. Walter, E. L. Warren, J. R. McKone, S. W. Boettcher, Q. Mi, E. A. Santori and N. S. Lewis, *Chem. Rev.*, 2010, **110**, 6446–6473

[3] X. Chen, S. Shen, L. Guo and S. S. Mao, *Chem. Rev.*, 2011, **110**, 6503–6570

[4] A. Fujishima and K. Honda, *Nature*, 1972, **238**, 37–38

[5] D. Barreca, G. Carraro, V. Gombac, A. Gasparotto, C. Maccato, P. Fornasiero, E. Tondello, *Adv. Funct. Mater.*, 2011, **21**, 2611-2623.

[6] W. Cristino, S. Caramori, R. Argazzi, L. Meda, G. L. Marra and C. A. Bignozzi, *Langmuir*, 2011, **27**, 7276–7284

[7] B. Cole, B. Marsen, E. Miller, Y. Yan, B. To, K. Jones and M. Al-Jassim, *J. Phys. Chem. C*, 2008, **112**, 5213–5220

[8] Y. S. Hu, A. Kleiman-Shwarsctein, A. J. Forman, D. Hazen, J. N. Park and E. W. McFarland, *Chem. Mater.*, 2008, **20**, 3803–3805

[9] D. K. Zhong, J. Sun, H. Inumaru and D. R. Gamelin, *J. Am. Chem. Soc.*, 2009, **131**, 6086–6087

[10] G. Carraro, C. Maccato, A. Gasparotto, T. Montini, S. Turner, O.O. Lebedev, V. Gombac, G. Adami, G. G. van Tendeloo, D. Barreca, P. Fornasiero, *Adv. Funct. Mater.*, 2014, **24**, 372.

[11] D. Barreca , P. Fornasiero , A. Gasparotto , V. Gombac , C. Maccato, T. Montini , E. Tondello, *ChemSusChem*, 2009, **2**, 230.

[12] C. -C. Hu, J. -N. Nian, H. Teng, *Sol. Energy Mater. Sol. Cells*, 2008, **92**, 1071.

[13] J. -N. Nian, C. -C. Hu, H. Teng, *Int. J. Hydrogen Energy*, 2008, **33**, 2897.

[14] T. W. Kim, H. -W. Ha, M. -J. Paek, S. -H. Hyun, J. -H. Choy, S. -J. Hwang, *J. Mater. Chem.*, 2010, **20**, 3238.

[15] J. Zhengbo, C. Tao, X. Jinyan; G. Lu, J. Ye, Y. Bi, *Sci. Reports*, 2013, **3**, 2720.

[16] Y. Li, L. Zhang, A. Torres-Pardo, J. M. Gonzales-Calbet, Y. Ma, P. Oleynikov, O. Terasaki, S. Asahina, M. Shima, D. Cha, L. Zhao, K. Takanabe, J, Kubota, K. Domen, *Nature Commun.*, 2013, **4**, 2566.

[17] A.T. Garcia-Esparza, D. Cha, Y. Ou, J. Kubota, K. Domen, K. Takanabe, *ChemSusChem*, 2013, **6**, 168-181.

[18] K. Takanabe and K. Domen, *ChemCatChem*, 2012, **4**, 1485-1497.

[19] D. I. Kondarides, V. M. Daskalaki, A. Patsoura, X. E. Verykios, *Catal. Lett.*, 2008, **122**, 26.

[20] M. Bowker, *Catal. Lett.* 2012, **142**, 923.

[21] X. Fu, J. Long, X. Wang, D. Y. C. Leung, Z. Ding, L. Wu, Z. Zhang, Z. Li, X. Fu, *Int. J. Hydrogen Energy,* 2008, **33**, 6484.

[22] T.V. Pham, M. Rao, P. Andreasson, Y. Peng, J. Wang, K.B. Jinesh, *Appl. Phys. Lett.*, 2013, **102**, 032101.

[23] A. Mittiga, E. Salza, F. Sarto, M. Tucci, and R. Vasanthi, *Appl. Phys. Lett.*, 2006, **88**, 163502.

[24] S. C. Ray, *Sol. Energy Mater. Sol. Cells*, 2001, **68**, 307.

[25] A. A. Ogwu, E. Bouquerel, O. Ademosu, S. Moh, E. Crossan, and F. Placido, *J. Phys. D: Appl. Phys.*, 2005, **38**, 266.

[26] J. F. Pierson, A. Thobor-Keck, and A. Billard, *Appl. Surf. Sci.*, 2003, **210**, 359.

[27] F. Marabelli, G. B. Parravicini, and F. Salghetti-Drioli, *Phys. Rev. B*, 1995, **52**, 1433.

[28] W. Siripala, A. Ivanovskaya, T.F. Jaramillo, S.H. Baeck and E.W. McFarland, *Sol. Energy Mater. Sol. Cells*, 2003, **77**, 229-237

[29] Z. Jin, X. Zhang, Y. Li, S. Li, G. Lu, *Catal. Commun.* 2007, **8**, 1267.

[30] H.-J.Choi, M. Kang, *Int. J. Hydrogen Energy*, 2007, **32**, 3841.

[31] V. Gombac, L. Sordelli, T. Montini, J. J. Delgado, A. Adamski, G. Adami, M. Cargnello, S. Bernal, P. Fornasiero, *J. Phys. Chem. A*, 2010, **114**, 3916.

[32] M. K. I. Senevirathna, P. K. D. D. P. Pitigala, K. Tennakone, *J. Photochem. Photobiol. A*, 2005, **171**, 257.

[33] Z. Zhang, P. Wang, *J. Mater. Chem.*, 2012, **22**, 2456.

[34] Q. Zhang, K. Zhang, D. Xu, G. Yang, H. Huang, F. Nie, C. Liu, S. Yang, *Progress in Mater. Sciences*, 2014, **60**, 208-337.

[35] T. Maruyama, *Sol. Energy Mater. Sol. Cells*, 1998, **56**, 85.

[36] J. Morales, L. Sanchez, F. Martin, J.R. Ramos-Barrado, M. Sanchez, *Thin Solid Films*, 2005, **474**, 133-140.

[37] L. Chen, S. Shet, H. Tang, H. Wang, T. Deutsch, Y. Yan, J. Turner and M. Al-Jassim, *J. Mater. Chem.*, 2010, **20**, 6962–6967.

[38] X. M. Liu and Y. C. Zhou, *Appl. Phys. A: Mater. Sci. Process.*, 2005, **81**, 685–689.

[39] M. Le, M. Ren, Z. Zhang, P. T. Sprunger, R. L. Kurtz and J. C. Flake, *J. Electrochem. Soc.*, 2011, **158**, E45–E49.

[40] D. P. Singh, N. R. Neti, A. S. K. Sinha and O. N. Srivastava, *J. Phys. Chem. C*, 2007, **111**, 1638–1645.

[41] J. G. Becerra, R. C. Salvarezza and A. J. Arvia, *Electrochim. Acta*, 1988, **33**, 613–621

[42] T.V. Pham, M. Rao, P. Adreasson, Y. Peng, J. Wang, K.B. Jinesh, *Appl. Phys. Lett.*, 2013, **102**, 032101.

[43] S.K. Kumar, S. Murugesan, S. Suresh, S.P. Raj, *J. Solar Energy*, 2013, 147270.

[44] N.G. Elfadill, M.R. Hasim, K.M. Chahrour, M.A. Qaeed, W. Chunsheng, *J. Mater. Sci: Mater. Electron.*, 2014, **25**, 262-266.

[45] K. Lim, J. Park, D.-G. Kim, J.-K. Kim, J.-W. Kang, Y.-C. Kang, *Appl. Surf. Sci.*, 2012, **258**, 9054-9057.

[46] M.H. Prasad Reddy, J.F. Pierson, S. Uthanna, *Phys. Status Solidi A*, 2012, **209**, 1279-1286.

[47] T.V. Pham, M. Rao, P. Adreasson, Y. Peng, J. Wang, K.B. Jinesh, *Appl. Phys. Lett.*, 2013, **102**, 032101.

[48] S. Ghosh, D.K. Avasthi, P. Shah, V. Ganesan, A. Gupta, D. Sarangi, R. Bhattacharaya, W. Assmann, *Vacuum*, 2000, **57**, 377-385.

[49] K. Lim, J. Park, D.-G. Kim, J.-K. Kim, J.-W. Kang, Y.-C. Kang, *Appl. Surf. Sci*., 2012, **258**, 9054-9057.

[50] N. Strataki, V. Bekiari, D.I. Kondarides, P. Lianos,. *App. Catal., B.* 2007, **77**, 184

[51] S. Y. Reece, J. A. Hamel, K. Sung, T. D. Jarvi, A. J. Esswein, J. J. H. Pijpers, and D. G. Nocera, *Science*, 2011, **334**, 645.

[52] Drera, G.; Salvinelli, G.; Åhlund, J.; Karlsson, P. G.; Wannberg, B.; Magnano, E.; Nappini, S.; Sangaletti, L., *J. Electron Spectrosc. Relat. Phenom*.**,** 2014*,* **195**, 109-116.

[53] a) M. P. Marder, *Condensed Matter Physics*, 2nd Edition, Wiley, 2010, Par.23.6.3 and Refs. therein; b) F. Parmigiani and L.Sangaletti, *J. Electron Spectrosc. Relat. Phenom*.**,** 1994*,* **66**, 223-239.

[54] a) I. Platzman, R. Brener, H. Haick, R. Tannebaum, *J. Phys. Chem. C*, 2008, **112**, 1101; b) J. Park, K. Lim. R.D. Ramsier, Y.-C. Kang, *Bull. Korean Chem. Soc*., 2011, **32**, 3395.

[55] J.A. Thornton, *J. Vac. Sci. Technol. A*, 1986, **4**, 3059.

[56] R. Messier, R.C. Ross, *J. Appl. Phys.*, 1982, **53**, 6220.

[57] E. Quartarone, P. Mustarelli, S. Grandi, F. Marabelli, E. Bontempi, *Journal of Vacuum Science and Technology A*, 2007, **25**, pp. 485-491.

[58] T. Kawai, T. Sakata, *JCS Chem. Comm.*,1980, 694.

[59] T. Kawai, T. Sakata, *Chem. Lett.*, 1981, **10**, 81.

[60] T. Sakata, Y. Kawai, *Chem. Phys. Lett*., 1981, **80**, 341.

[61] T. Sakata, T. Kawai, K. Hashimoto, *Chem. Phys. Lett*., 1982, **88**, 50.

[62] J. Chen, D.F. Ollis, W.H. Rulkens, H. Bruning, *Water Research*, 1999, **33**, 669.

[63] H.J. Choi, M. Kang, *Int. J. Hydrogen Energy*, 2007, **32**, 3841.

[64] L.S. Yoong, F.K. Chong, B.K. Dutta, *Energy*, 2009, **34**, 1652.

[65] T. Chen, Z.C. Feng, G.P. Wu, J.Y. Shi, G.J. Ma, P.L. Ying, *J. Phys. Chem*. 2007, **111**, 8005.

[66] T. Chen, G.P. Wu, Z.C. Feng, G.S. Hu, W.G. Su, P.L. Ying, et al., *Chinese J. Cataly*., 2008, **29**, 105.

[67] V. Gombac, L. Sordelli, T. Montini, J. J. Delgado, A. Adamski, G. Adami,M. Cargnello, S.

Bernal, P. Fornasiero, *J. Phys. Chem. A*, 2010, **114**, 3916 –3925

[68] L. Huang et al., *Solid State Sciences*, 2009, **11**, 129-138.

[69] D. Barreca, P. Fornasiero, A. Gasparotto, V. Gombac, C. Maccato, T. Montini and E. Tondello, *ChemSusChem*, 2009, **2**, 230-233.

[70] C. Maccato, D. Barreca, G. Carraro, A. Gasparotto, V. Gombac, P. Fornasiero, *Surface & Coatings Technology*, 2013, **230**, 219-227.

[71] G. Carraro, A. Gasparotto, C. Maccato, V. Gombac, F. Rossi, T. Montini, D. Peeters, E.Bontempi, C. Sada, D. Barreca, P. Fornasiero, *RSC Advances,* 2014, **4**, 32174-32179.